



PERGAMON

Acta mater. 48 (2000) 3211–3220



www.elsevier.com/locate/actamat

ANALYSIS OF A WEDGE IMPRESSION TEST FOR MEASURING THE INTERFACE TOUGHNESS BETWEEN FILMS/COATINGS AND DUCTILE SUBSTRATES

M. R. BEGLEY^{1†}, D. R. MUMM², A. G. EVANS² and J. W. HUTCHINSON³

¹Mechanical Engineering Department, University of Connecticut, Storrs, CT 06269, USA, ²Materials Institute, Princeton University, Princeton, NJ 05840, USA and ³Division of Engineering and Applied Science, Harvard University, Cambridge, MA 02138, USA

(Received 13 August 1999; accepted 10 April 2000)

Abstract—The adhesion between thin elastic films/coatings and ductile substrates can be measured using a wedge test, wherein a long sharp edge is impressed through the film into the substrate. The resulting plastic deformation causes delamination between the film and the substrate. The extent of the delamination can be correlated with the crack driving force to determine the toughness of the interface. Results are presented that relate the energy release rate and mode-mixity to the stresses: both residual and those induced by the impression. Numerical and asymptotic results are presented for the strain transferred to the coating. The numerical results verify that the asymptotics provide accurate closed-form solutions when the delaminations exceed about seven contact widths. An example is provided for a thermal barrier coating system. © 2000 Acta Metallurgica Inc. Published by Elsevier Science Ltd. All rights reserved.

Keywords: Interface; Fracture toughness; Multi-layers; Indentation

1. INTRODUCTION

Impression tests have emerged as a relatively straightforward method for measuring the adhesion of films and coatings on ductile substrates, particularly on structural alloys. Methods based on spheres [1–3], cones [4] and wedges [5] have been developed and used primarily for thin film interface adhesion measurements. To apply such tests, the indenter is impressed through the film into the substrate to induce plastic penetration, as illustrated in Fig. 1. This causes an interface delamination that spreads out from the impression as the depth increases. The interface toughness is obtained by measuring the size of the delamination as a function of the impression load.

Among the impression geometries, wedges have several advantages. The driving force for delamination is largest, allowing testing of systems with more adherent interfaces. Plane-strain conditions eliminate the tensile stresses parallel to the delamination crack front that cause radial cracking. The plane surface of the wedge may be used as a mirror, allowing *in situ* optical measurements of crack growth [6].

The present article extends an introductory study of the wedge method [5] with two principal objectives:

- (i) To establish a testing domain that allows application of a straightforward, broadly applicable closed-form solution.
- (ii) To apply the method to multi-layers. A specific example is given for a thermal barrier coating (TBC) which comprises a thin layer of Al_2O_3 ($\approx 3 \mu\text{m}$) and a thick layer of compliant ZrO_2 ($\approx 100 \mu\text{m}$) having the properties listed in Table 1.

Experimental measurements made on a TBC [6] provide a context for the analysis. A typical optical image of an impressed system (see Fig. 2) indicates the contrast associated with delamination. Measurements of the delamination length, a , and the impression load (or impression width) permit determination of the interface toughness, as elaborated upon below.

Surface strains are determined by a combination of numerical calculations and analytical results. These strains are considered to transmit to the coating and superpose on the residual strains. This approach has been used [1, 4] and verified by means of detailed finite element models [3]. The total strains are subsequently

† To whom all correspondence should be addressed.

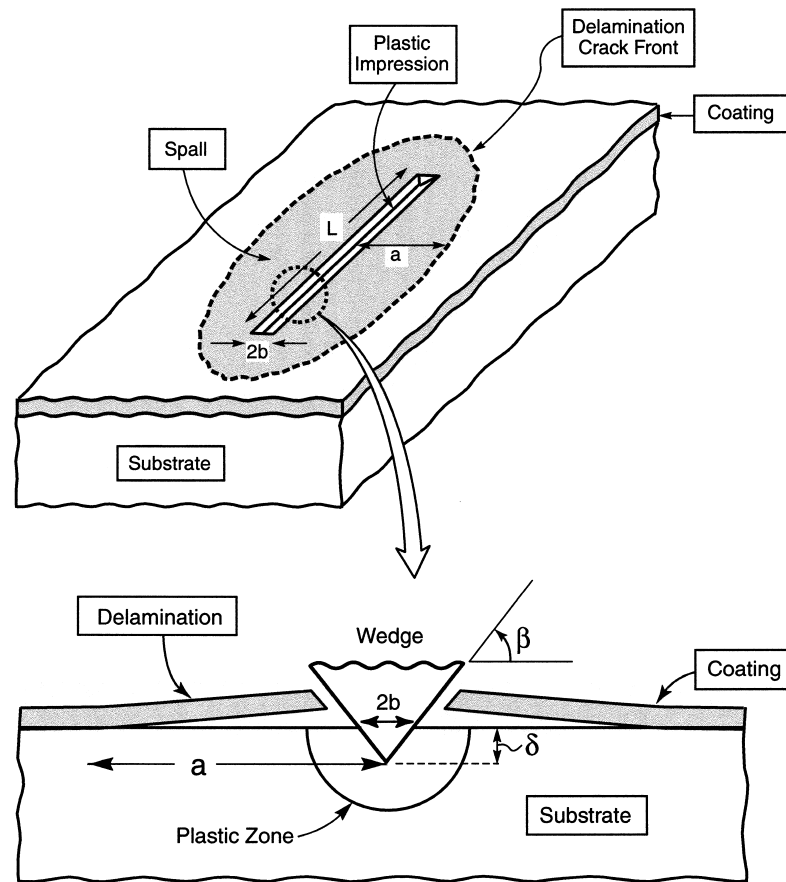


Fig. 1. Schematic diagram of the wedge or cone impression test.

used with a multi-layer model to determine the energy release rate as a function of delamination length. In this respect, the analysis extends that from previous studies [4, 5].

Closed-form analytical solutions, similar to those set forth by Vlassak *et al.* [5], are derived for both conical and wedge geometries and compared with new finite element results. The numerical results illustrate that the asymptotics accurately capture the behavior remote from the plastic zone, particularly for the wedge geometry. These expressions eliminate the need for detailed numerical results when the delaminations are long compared with the impression width. The influence of thickness and stiffness of the elastic film on the solutions is also explored using finite element models.

2. SURFACE STRAINS

The impression test is modeled as an elastic layer bonded to an elastic-plastic substrate. The response of the substrate is characterized using conventional J_2 flow theory; this representation is essential for accurate predictions of the strain near the surface (e.g. Ref. [1]). The uni-axial behavior of the material is considered to follow an isotropic Ramberg-Osgood strain hardening relationship:

$$\varepsilon = \frac{\sigma}{E_s} + \alpha \left(\frac{\sigma}{\sigma_y} \right)^n \quad (1)$$

where E_s is the Young's modulus of the substrate, σ_y is its yield strength, n is the hardening exponent, and α is a parameter which controls the relative

Table 1. Properties of a thermal barrier coating bilayer system comprised of α - Al_2O_3 and c- Zr_2O_3

Layer	Layer thickness (μm)	In-plane modulus (GPa)	Thermal expansion coefficient (p.p.m.)
α - Al_2O_3	1–5	380	8
c- Zr_2O_3	100–200	5–20 (13 ^a)	12.6
Substrate	3000	200	15–18

^a Value determined from curvature measurements [6].

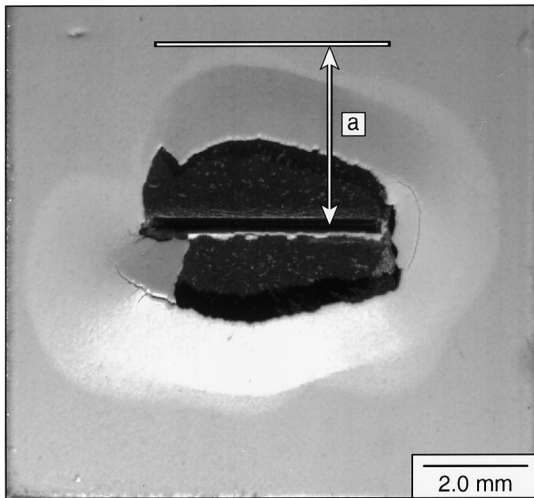


Fig. 2. Typical optical image of an impressed TBC system. The impression area of the wedge appears as a solid dark line. The delamination distance is approximately 25 times the impression size of 30 μm .

contribution of the inelastic strain. The yield strain is taken as: $\epsilon_y = \sigma_y/E_s$. The surface strains are calculated using the finite element models developed in the commercial code ABAQUS. The plasticity and contact modeling follow standard procedures; details are included in the Appendix.

The results are presented in terms the hardness, H , which is defined as the indenter load divided by the contact area of the impression. The hardness values we report in Table 2 are based on the finite element results. Alternatively, the material hardness can be estimated using closed-form relationships set forth by Johnson [7, 8]. These relationships predict the classical result that $H \approx (3 - 4)\sigma_y$, which is only accurate when strain-hardening is limited.

2.1. Thin compliant films

Thin and/or compliant films do not influence the substrate deformation except for a very small region near the edge of contact. With the assumption that the strain at the surface of the substrate is transmitted to the film as a uniform strain in the thickness direction[†], the strain in the film can be determined from impression results obtained for just the elastic-plastic substrate. Results are shown in Fig. 3 for a typical yield strain and for several values of hardening exponent. Since the details of the deformation in the actual contact zone are not of interest here, they are not shown in the figure.

When the interface crack propagates several con-

[†] This assumption is supported by finite element models that explicitly model the film, both those presented here and the more extensive calculations in Ref. [3].

[‡] See also Ref. [3].

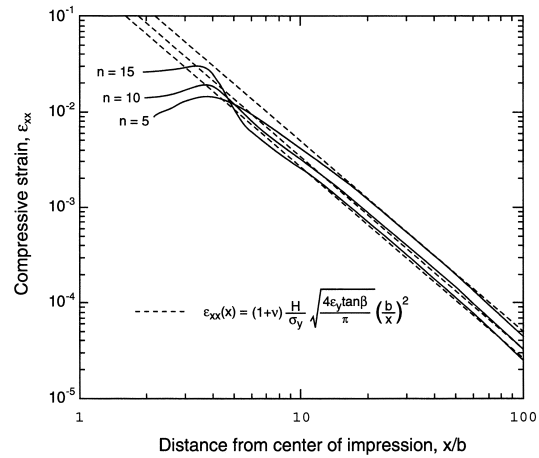


Fig. 3. Surface strain distributions along the surface of the substrate for cases where the role of the film has been neglected.

tact sizes away from the center of the impression, the asymptotic surface strain distribution (described in Section 2.3) can be exploited to simplify the analysis. The strain far from the impression varies with distance, x , in accordance with

$$\epsilon_{xx}(x) = \epsilon_0 \left(\frac{b}{x}\right)^2 \tag{2}$$

where b is the half-width of the impression.

When the contact area is much greater than the tip radius of the wedge, the self-similarity of the impression process dictates that the strain coefficient ϵ_0 be independent of the impression size. This simply means that the strains scale with the impression size according to equation (2), and that ϵ_0 is a function of non-dimensional material properties only: $\epsilon_0 = f(n, \epsilon_y, \alpha)$. Numerical results for a variety of material properties are provided in Table 2.

2.2. Stiff or thick films

For stiff films or shallow impressions, the film may affect the plastic deformation and limit the substrate strains transferred to the film. The presence of the film introduces an additional length scale that removes the self-similarity of the deformation, such that the shape of the strain distribution becomes dependent on impression size relative to the film thickness. Strain distributions at the film-substrate interface have been calculated for several values of film thickness and modulus, at a constant impression size (see Fig. 4), with the portion of the film directly under the impression removed. (In practice, this region experiences extensive cracking and spalling [6].) It is evident that, if the impression size is about an order of magnitude larger than the film thickness, h , the film has minimal influence[‡]. Conversely, thicker films affect the

Table 2. Finite element results and asymptotic predictions for 90° and 120° wedges for several values of plastic properties

Properties	90° Wedge						120° Wedge				
	n	ε_y	α	c/b	H/σ_y^a	ε_0 fit to FEA	ε_0 equation (5)	c/b	H/σ_y^a	ε_0 fit to FEA	ε_0 equation (5)
	5	0.01	0.03	5.79	8.83	0.50	0.66	4.40	7.45	0.26	0.43
	10	0.01	0.03	5.79	5.39	0.41	0.41	4.40	4.93	0.25	0.28
	15	0.01	0.03	5.79	4.35	0.35	0.33	4.40	4.00	0.22	0.23
	5	0.005	0.03	8.19	9.47	0.47	0.53	6.22	8.97	0.25	0.36
	10	0.005	0.03	8.19	6.11	0.35	0.33	6.22	4.39	0.22	0.22
	15	0.005	0.03	8.19	4.88	0.26	0.26	6.22	4.50	0.19	0.19
	5	0.0025	0.03	11.58	10.41	0.31	0.392	8.80	9.80	0.19	0.28
	10	0.0025	0.03	11.58	6.51	0.23	0.245	8.80	6.09	0.17	0.17
	15	0.0025	0.03	11.58	5.01	0.16	0.19	8.80	4.87	0.13	0.14
	10	0.005	0.003	8.19	7.45	0.35	0.40				
	10	0.005	0.03	8.19	6.11	0.35	0.33				
	10	0.005	0.3	8.19	4.77	0.27	0.25				

^a Hardness is defined as $H = L/2b$ where L is the indenter load per unit length.

deformation, such that the region where equation (2) is valid is pushed further from the center of the impression, as illustrated in Fig. 4.

2.3. Asymptotic analysis

The spatial dependence of equation (2) is predicted by an approximate analysis, wherein it is assumed that a semi-cylindrical plastic core forms underneath the impression. The asymptotic analysis presented here is very similar to that set forth by Vlassak *et al.* [5]; some of the same results are presented here, both for completeness and to provide the basis for comparisons with new explicit numerical models. The analysis is based on the assumptions that a plastic zone expands from the center of contact by purely radial displacements, and the material is incompressible in the plastic zone (e.g. Refs [7, 8]). The strain in the elastic region is given by

$$\varepsilon_{xx}(x) = \varepsilon'_0 \left(\frac{c}{b}\right)^2 \left(\frac{b}{x}\right)^2 \quad (3)$$

where c is the size of the plastic zone and ε'_0 is a constant. An estimate for the size of the zone is given by Johnson [7] as

$$\frac{c}{b} \cong \sqrt{\frac{4 \tan \beta}{\pi(5-4\nu)\varepsilon_y}} \quad (4)$$

where β is the angle between the surface and the indenter (see Fig. 1). The constant ε'_0 is determined from the pressure acting at the outer edge of the plastic zone, which can be related to the indentation load over the contact area, or hardness. Equation (3) becomes

$$\varepsilon_{xx}(x) = (1-\nu) \left(\frac{H}{\sigma_y}\right) \sqrt{\frac{4\varepsilon_y \tan \beta}{\pi}} \left(\frac{b}{x}\right)^2. \quad (5)$$

It should be noted that this asymptotic behavior occurs outside the plastic zone. As such, equation (4) is a fairly accurate estimate for the minimum

distance at which the asymptotic result applies. The values for ε_0 determined via equation (5) are compared in Table 2 with values determined via fitting equation (2) to the FEA results. For a wide range of substrate plastic properties, the agreement is excellent.

The assumption that deformation occurs in a purely radial manner depends strongly on the shape of the impression, the amount of strain hardening and the yield strain. For either sharp impressions, small amounts of strain hardening, or low yield strains, the FEA results illustrate that piling up around the edge of the impression is more pronounced and the edge of the plastic zone takes on a non-circular shape. Conversely, for large amounts of strain hardening or high yield strains, plastic deformation is reduced and elastic contributions are more important. These effects ultimately dictate the accuracy of the asymptotic expression for ε_0 [i.e. the term multiplying $(b/x)^2$ in equation (5)].

It is interesting to note that regardless of these specific details of the plastic zone beneath the

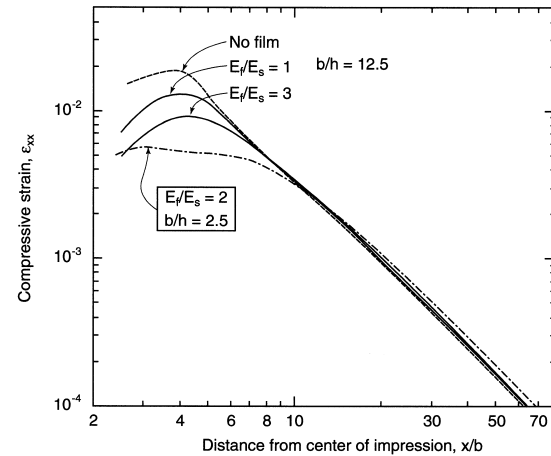


Fig. 4. Surface strain distributions along the interface (surface of the substrate) for cases where the film has been explicitly modeled.

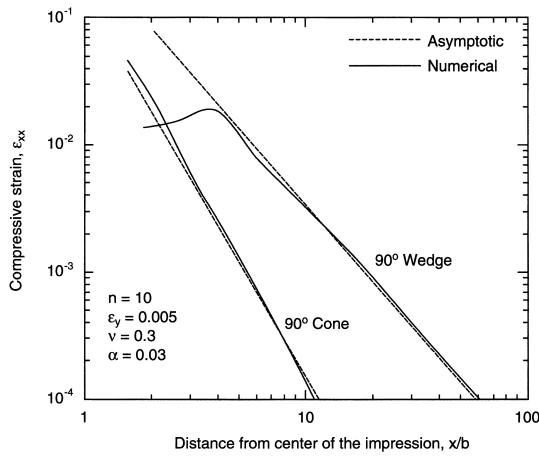


Fig. 5. Comparison of surface strain distributions for 90° wedges and cones, with asymptotic predictions outlined in the text.

wedge, the surface strain distribution in the elastic region is still characterized by the $(b/x)^2$ distribution, as illustrated in Figs 3 and 4. This is because the strain along the surface is governed by the dilatation needed to accommodate the indenter†. An alternative yet similar approach to predicting the strain distribution further emphasizes the role of dilation, as this second asymptotic prediction is independent of the plastic properties of the substrate. This approach is outlined in the Appendix, and is most valid for soft materials.

These asymptotic expressions are restricted to plane-strain deformation. Accordingly, in applying these results to finite-width wedges, it is important that the delamination distance not exceed the length of the wedge. As such, the delamination shown in Fig. 2 exceeds this size and the present results would only be applied in an approximate sense.

2.4. Comparison with conical impressions

The asymptotic strain distribution for the cone (see Fig. 5) varies with $1/x^3$ (compared with $1/x^2$ for the wedge) such that, in the elastic region

$$\epsilon_{rr}(x) = (1 + \nu) \left(\frac{H}{\sigma_y} \right) \left(\frac{\epsilon_y^2 \tan \beta}{6(1 - \nu)} \right)^{1/3} \left(\frac{b}{x} \right)^3 \quad (6)$$

This solution is obtained by applying the same procedure presented in the previous section and upon

† Note that a purely vertical load does not cause a surface strain parallel to the surface, while a surface load applied tangential to the surface results in the same asymptotic distribution given by equation (5) [8].

‡ As a result of this assumption, the results presented here will asymptote to the same limit predicted in Ref. [4] for conical impression. See Fig. 1.

using the results provided by Johnson [7]. The extent of the plastic boundary is estimated as

$$\frac{c}{b} \cong \left[\frac{\tan \beta}{6(1 - \nu)\epsilon_y} \right]^{1/3} \quad (7)$$

Again, equation (7) provides a useful estimate for the distance away from the impression beyond which equation (6) can be used. Detailed results for strains near the impression are presented [4].

A comparison between asymptotic and numerical results is provided in Fig. 5 for both a conical and wedge impression. Note that, near the impression, the conical deformation transmits a greater strain than the wedge deformation. However, even at a small distance from the edge of contact, the wedge imparts larger strains, and continues to do so out to very large distances.

3. DELAMINATION MECHANICS

3.1. Energy release rates

With the premise that the surface strain in the substrate is transmitted to the coating as a uniform compression (independent of vertical location in the film), the energy release rate, G , can be evaluated for any multi-layer coating. The analysis assumes that G is governed by the strain at the surface site coincident with the delamination front. Here, the result for a bilayer is derived and reduced to the monolayer solution. A numerical program exists for multilayers [9]. The bilayer result for the steady-state energy release rate is [10]

$$G = \frac{1}{2} P \Delta \epsilon - \frac{1}{2} M \Delta \kappa \quad (8)$$

where P is the net force acting on the layer before decohesion, and M is the net moment referenced to the neutral axis of the layer, again before decohesion. The quantity $\Delta \epsilon$ is the strain change at the neutral axis of the layer, caused by decohesion, while $\Delta \kappa$ is the curvature change. (For most cases, the curvature change is simply that resulting from thermal expansion mismatch.) The strain and curvature changes can be calculated from elementary strength of materials applied to the decohered layer, under the restriction that the net force and net moment acting on the released layer are zero. The residual strain parallel to the debond front is not relieved during the delamination‡.

The relevant results for a bilayer with thicknesses h_1 and h_2 are

$$P = E_1' h_1 [(1 + \nu_1)\epsilon_{1r} + \epsilon_i] + E_2' h_2 [(1 + \nu_2)\epsilon_{2r} + \epsilon_i] \quad (9)$$

where ϵ_{1r} and ϵ_{2r} are residual strains in the respective layers and ϵ_i is the strain transferred to the layer as a result of the substrate deformation [note that it

will be a function of position defined by equation (2)]. The quantities E'_1 and E'_2 are the plane strain moduli of the layers, that is $E'_1 = E_1/(1 - \nu_1^2)$ and $E'_2 = E_2/(1 - \nu_2^2)$. The moment M (referenced to the neutral axis of the released layer) is given by

$$M = -\frac{E'_1 E'_2 h_1 h_2 [(1 + \nu_1)\varepsilon_{1r} - (1 + \nu_2)\varepsilon_{2r}]}{2(E'_1 h_1 + E'_2 h_2)}. \quad (10)$$

The curvature change of the released layer is

$$\Delta\kappa = \frac{6[(1 + \nu_1)\varepsilon_{1r} - (1 + \nu_2)\varepsilon_{2r}]}{h_1} \left(\frac{1 + h_1/h_2}{\xi} \right) \quad (11)$$

where the non-dimensional function ξ is given as

$$\xi = \frac{E'_1}{E'_2} \left(\frac{h_1}{h_2} \right)^2 + \frac{E'_2}{E'_1} \left(\frac{h_2}{h_1} \right)^2 + 4 \left(\frac{h_2}{h_1} \right) + 4 \left(\frac{h_1}{h_2} \right) + 6. \quad (12)$$

Note that the curvature depends only on the difference in residual strains. It is unaffected by the wedge-induced strains. In turn, the residual strain difference is governed by the thermal expansion misfit, as elaborated upon in Section 4.

The strain change at the neutral axis of the layer is

$$\Delta\varepsilon = \frac{E'_1 h_1 [(1 + \nu_1)\varepsilon_{1r} + \varepsilon_i] + E'_2 h_2 [(1 + \nu_2)\varepsilon_{2r} + \varepsilon_i]}{E'_1 h_1 + E'_2 h_2}. \quad (13)$$

For simplicity of presentation and also to facilitate the mode-mixity analysis described in the next

$$\Gamma_i = \frac{\left(E'_1 h_1 (1 + \nu_1)\varepsilon_{1r} + E'_2 h_2 (1 + \nu_2)\varepsilon_{2r} + (E'_1 h_1 + E'_2 h_2)\varepsilon_0 \left(\frac{b}{a} \right)^2 \right)^2}{2(E'_1 h_1 + E'_2 h_2)} - \frac{M\Delta\kappa}{2} \quad (18a)$$

section, it is convenient to represent the bilayer as a single layer with an effective plane-strain modulus, E'_e , and an effective thickness, h_e . The modulus and the thickness of the single layer are defined such that its stretching and bending stiffness are identical to those of the bilayer, with the proviso that M for the single layer is taken about its own centerline. This implies that

$$E'_e h_e \Delta\varepsilon = P \quad (14a)$$

and

$$\frac{E'_e h_e^3 \Delta\kappa}{12} = -M. \quad (14b)$$

Solving equations (14a) and (14b), with equations (11) and (12), for E'_e and h_e gives

$$h_e \equiv \sqrt{\frac{-M\Delta\varepsilon}{P\Delta\kappa}} = \frac{h_1 \left(\frac{E'_2 \xi}{E'_1} \right)^{1/2}}{\left(\frac{h_1}{h_2} + \frac{E'_2}{E'_1} \right)}. \quad (15)$$

The corresponding effective plane strain modulus is

$$E'_e \equiv \frac{P}{h_e \Delta\varepsilon} = E'_1 \frac{\left(1 + \frac{E'_1 h_1}{E'_2 h_2} \right)^2 \left(\frac{h_1}{h_2} \right)}{\left(\xi \frac{E'_1}{E'_2} \right)^{1/2}}. \quad (16)$$

The energy release rate expressed in terms of the effective properties is

$$G = \frac{1}{2} \frac{P^2}{E'_e h_e} + 6 \frac{M^2}{E'_e h_e^3}. \quad (17)$$

Given the definition of the modulus and thickness of the single effective layer, the energy release rate expressed as equation (17) is identical to the original expression (8) for the bilayer.

The above expressions, together with the impression strain (2), are used to calculate the energy release rate in the wedge test as a function of delamination length, a . The interface toughness, Γ_i , is then obtained upon equating G in equation (8) to Γ_i and upon equating ε_{xx} from equation (2) with ε_i . After rearranging, the interface toughness becomes

where M is given by equation (10), and $\Delta\kappa$ must be estimated or measured experimentally.

For a single layer, the above expression reduces to

$$\frac{\Gamma_i}{Eh} = \frac{(1 + \nu)}{2(1 - \nu)} \left(\varepsilon_r + \frac{\varepsilon_0}{(1 + \nu)} \left(\frac{b}{a} \right)^2 \right)^2. \quad (18b)$$

Note that the delamination length a (for a fixed interface toughness) is proportional to the impression half-width, b . Recall that these expressions are not expected to be accurate when the delamination length substantially exceeds the wedge length.

The relationships between the interface toughness

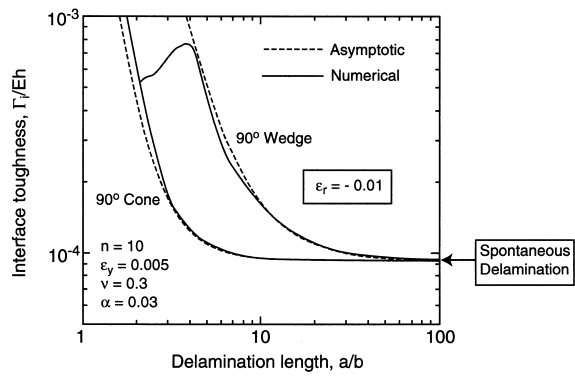


Fig. 6. Energy release rates for a single layer for both cone and wedge indents, including FEA predictions and the asymptotic predictions outlined in the text.

and delamination length for a single layer film are displayed as Fig. 6. Full numerical results as well as the closed form given as equation (18b) are shown for both cone and wedge impressions. Far from the impression, the curves approach the limit for spontaneous edge spalling due to the residual stresses alone. The corresponding relationships for a bilayer system, determined from equation (18a) are presented in Fig. 7, for three levels of residual strain in the bottom film, ε_{1r} , using the normalization $\Gamma_i/(E_e' h_e)$. The layer properties used in Fig. 7 correspond to the bilayer system discussed in subsequent sections. These results are used below to assess the interface toughness for a TBC system.

3.2. Mode mixity

Since the interface toughness depends on mode-mixity, it is of interest to determine the mode I and mode II stress intensity factors. An exact solution for the bilayer cannot be obtained without resorting to numerical methods. However, an approximate solution can be developed by replacing the bilayer with the single “effective” layer.

For a single layer (in this case having the effective properties defined earlier), the mode-mixity is given by the standard decomposition [10]:

$$K_I = \frac{P}{\sqrt{2h_e}} \cos(\omega) + \frac{\sqrt{6}M}{\sqrt{h_e^3}} \sin(\omega) \quad (19a)$$

and

$$K_{II} = \frac{P}{\sqrt{2h_e}} \sin(\omega) - \frac{\sqrt{6}M}{\sqrt{h_e^3}} \cos(\omega) \quad (19b)$$

† The curvature expression used in this procedure was similar to equation (11), but based on the assumption that the residual strain parallel to the decohesion direction was unconstrained, since the measurement was taken on a layer that was removed from the substrate.

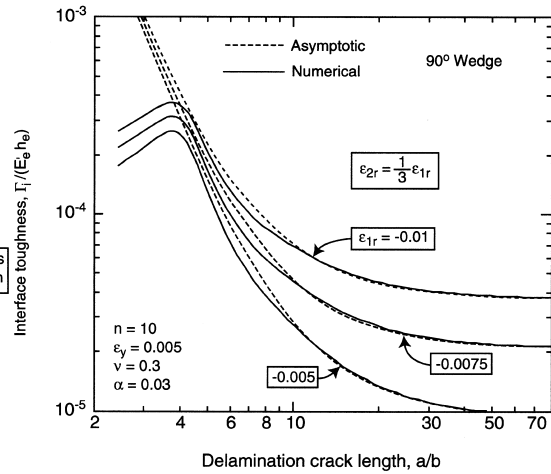


Fig. 7. Energy release rate distributions for the representative bilayer case considered in Section 4.

where ω is a function of the elastic properties of the bottom layer and substrate. For a wide range of material systems, $\omega \approx 52^\circ$. The phase angle of the interface crack is given by

$$\psi \equiv \tan^{-1} \left(\frac{K_{II}}{K_I} \right). \quad (19c)$$

This representation is exact for the case of a single layer; it is being used here as an approximation to the bilayer case. It should be noted that the delamination is open when $K_I > 0$; otherwise, it is closed and $\psi = \pm 90^\circ$. Note that the impression strain decreases the mode I component of the energy release rate, since it elevates the compressive edge load. Conversely, bending opens the crack and lowers the phase angle, as illustrated in Fig. 8.

4. ILLUSTRATION: APPLICATION TO A THERMAL BARRIER COATING

Application of the wedge impression test is illustrated for a TBC system discussed elsewhere [6]. The material properties and dimensions are listed in Table 1. The modulus of the porous top layer (ZrO_2) was determined to be $E_2 = 13$ GPa, by using the curvature measured on a fully decohered bilayer, knowing the layer thicknesses and modulus of the bottom layer (Al_2O_3)†. This direct measurement of E_2 minimizes the uncertainties otherwise attributed to variability and anisotropy. The relevant parameters for this system are (assuming values given in Table 1 and thicknesses $h_1 = 2.88 \mu m$ and $h_2 = 121.6 \mu m$):

$$\frac{h_e}{h_1} = 14.1 \quad (20a)$$

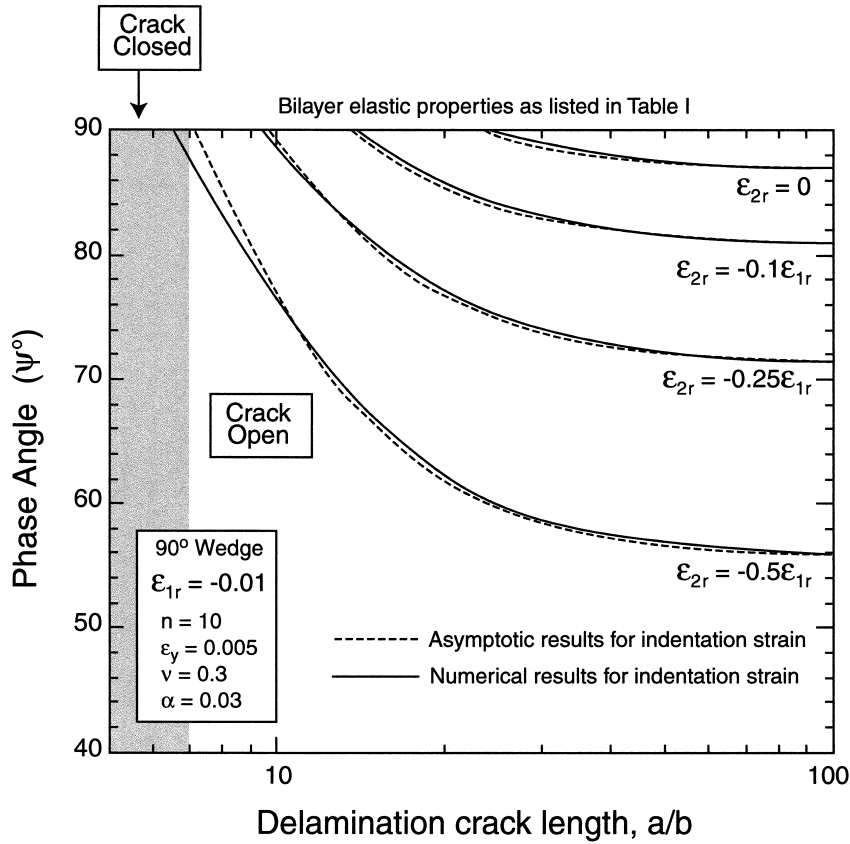


Fig. 8. Phase angle of the energy release rate for the same material properties and geometry as considered in Section 4, with different values of residual strain in the top layer.

$$\frac{E'_c}{E_1} = 0.17 \quad (20b)$$

$$\frac{G}{E_c h_c} = 0.373 \varepsilon_{1r}^2 + 0.822 \varepsilon_{1r} \varepsilon_i + 0.5 \varepsilon_i^2 \quad (20c)$$

$$\begin{aligned} \frac{K_I}{E'_c \sqrt{h_c}} &= (0.582 \varepsilon_{1r} + \sqrt{2} \varepsilon_i) \cos(\omega) \\ &- 0.189 \varepsilon_{1r} \sin(\omega) \end{aligned} \quad (20d)$$

and

$$\begin{aligned} \frac{K_{II}}{E'_c \sqrt{h_c}} &= (0.582 \varepsilon_{1r} + \sqrt{2} \varepsilon_i) \sin(\omega) \\ &- 0.189 \varepsilon_{1r} \cos(\omega). \end{aligned} \quad (20e)$$

Using the properties outlined in Table 1, the residual strains are approximately $\varepsilon_{1r} \approx -0.0076$ and $\varepsilon_{2r} \approx -0.0026$. Based on these parameters, the

† This reduction reflects the decrease due to the curvature term in equation (8).

interface toughness is found to be $\Gamma_i = 56 \text{ J/m}^2$. The phase angle is $\psi = 90^\circ$ (pure mode II), since the bending moment on the decohered layer is not large enough to open the crack.

To gain some appreciation of the principal source of the energy release rate, the separate contributions from the alumina and the TBC are examined, as well as the importance of bending of the decohered layer. Without bending, the crack driving force would be higher by about 10 J/m^2 †. Hence, the crack driving force is dominated by the higher residual strain and modulus of the bottom layer of Al_2O_3 . If the top zirconia layer is completely neglected, the energy release rate [via equation (18b)] would be $\Gamma_i = 52 \text{ J/m}^2$. Despite its thickness, the comparatively low modulus of the top layer limits the reduction due to bending. These values were computed using the low end of the range of the substrate thermal expansion coefficient given in Table 1. Using the high end would lead to a toughness of about 80 J/m^2 . This difference emphasizes the importance of accurately measuring residual stresses in the layers.

The toughness is higher than that for the adjoining Al_2O_3 ($\Gamma \approx 25 \text{ J/m}^2$), yet the delamination

remains at the interface. A rationale for this is given elsewhere [6]. Briefly, kinking of the crack into the Al_2O_3 is inhibited by a combination of factors, particularly the high modulus of the Al_2O_3 , and the presence of a large residual compression in this layer (3–4 GPa). Furthermore, there is an appreciable frictional contribution to Γ_i since the crack is closed and growing in pure mode II.

5. CONCLUSION

The wedge test provides a convenient, yet accurate, means of measuring the interface toughness. It is particularly straightforward for relatively weak interfaces that lead to large delamination lengths, such the behavior is accurately captured by closed-form expressions. The interface toughnesses implied from the impression test are a strong function of the residual strain present in the layer, as illustrated by Figs 6–8. Accurate measurements of this strain are an essential aspect of interface toughness determination. The utility of these methods has been demonstrated by analyzing measurements made on a thermal barrier coating.

REFERENCES

1. Begley, M. R., Evans, A. G. and Hutchinson, J. W., *Int. J. Solids Struct.*, 1999, **36**, 2773.
2. Wang, Y., Sugimura, Y., Evans, A. G. and Tredway, W. K., *Thin Solid Films*, 1999, **325**, 163.
3. Begley, M. R. and Jakubowski, M. A., to be published.
4. Drory, M. D. and Hutchinson, J. W., *Proc. R. Soc. Lond., Ser. A*, 1996, **452**, 2319.
5. Vlassak, J. J., Drory, M. D. and Nix, W. D., *J. Mater. Res.*, 1997, **12**, 1900.
6. Mumm, D. R. and Evans, A. G., *Acta mater.*, 2000, **48**, 1815.
7. Johnson, K. L., *J. Mech. Phys. Solids*, 1970, **18**, 115.
8. Johnson, K. L., *Contact Mechanics*. Cambridge University Press, Cambridge, 1985.
9. Bagchi, A., Lucas, G. E., Suo, Z. and Evans, A. G., *J. Mater. Res.*, 1994, **9**, 1734.
10. Hutchinson, J. W. and Suo, Z., *Adv. appl. Mech.*, 1991, **29**, 63.

APPENDIX

A.1. Numerical analyses

The wedge impression test is modeled as plane-strain line contact between a rigid indenter and an elastic–plastic half-space with a uni-axial stress–strain relationship given as equation (1) in the main body of the text. The tip of the indenter was rounded to improve convergence during the early stages of contact. The final impression width was at least 10 times the tip radius, and numerical studies indicated that the results away from the tip were self-similar and independent of indenter tip geometry. The outer boundary of the mesh was determined by increasing the size of the boundary until the surface strains became independent of mesh

geometry at a location of approximately 150 times the impression width. A series of convergence tests indicated that the strain distributions were independent of both mesh density and the size of the outer boundaries. The self-similarity of the solution (i.e. that the results can be scaled accurately by the impression size) was verified additionally by confirming that the predicted normalized hardness, H/σ_y , was independent of contact size.

Contact is modeled using an algorithm available in the code. The rigid indenter is modeled as a constraint on the surface displacement and enforced with a penalty method. The code uses internally generated gap elements to determine which nodes are in contact with the indenter at every load increment. Friction between the indenter and substrate was modeled with a Coulomb friction law, $\sigma_t = \mu\sigma_n$, where μ is the coefficient of friction, and σ_t , σ_n are the tangential and normal tractions at the contact interface, respectively. For slipping nodes, this relationship is enforced using Lagrange multipliers. The friction coefficient was taken as $\mu = 0.5$, which for the cases presented (i.e. relatively blunt indenters), results in strain distributions identical with sticking friction, except for locations very near the edge of contact.

Four-noded, reduced integration plane-strain hybrid elements were used. These elements include the hydrostatic component of stress as an additional degree of freedom. These elements avoid significant convergence difficulties that otherwise result as a result of the large hydrostatic stress generated by the nearly incompressible plastic deformation around the indenter. The models consisted of three to four elements in the contact zone near the rounded tip, 20 elements in the contact zone and 150 elements from the edge of contact to the outer boundary, which were biased towards the impression zone.

The coefficient controlling the strain magnitude in equation (2) was determined by a least-squares fit to the finite element data in the region defined by $c/b \leq x/b \leq 150$, where c/b is the closed-form estimate of the plastic zone size, given as equation (4). These results are presented in Table 2.

A.2. Alternative asymptotic form for strain

If one assumes that the indenter penetration (and hence, surface dilation) is accommodated *purely* by plastic deformation, and that pile-up (or sinking-in) is negligible, an expression similar to equation (5) can be derived with $(\delta/x)^2$ in place of $(b/x)^2$. This procedure involves estimating the plastic zone size via equation (4), relating the contact size to the indentation depth via the indenter geometry, and invoking the requirement that the edge of the plastic zone is exactly at yield (dictated by an elastic–perfectly plastic yield strain $\varepsilon_y = \sigma_y/E$). The asymp-

total strain distribution becomes

$$\varepsilon_{xx}(x) = \left(\frac{4(1-\nu^2)\tan\beta}{\pi\sqrt{3}(5-4\nu)} \right) \left(\frac{\delta}{x} \right)^2.$$

The finite element results support this approximation when the material is “soft”, with a small yield strain and moderate hardening exponent; when the results in Fig. 3 are re-plotted with this

normalization, they collapse to a single curve away from the center of the impression. However, the finite element models do indeed account for the downward displacement of the indenter due to elastic deformation, which strictly speaking is a function of the size of the mesh. Thus, agreement between numerical results and asymptotic forms based on indenter displacement can be somewhat sensitive to the dimensions of the mesh.